

Submitted to ApJ

# Interstellar Dust and Magnetic Field at the Heliosphere

Priscilla C. Frisch

*Department of Astronomy and Astrophysics, University of Chicago, Chicago, IL 60637.*

frisch@oddjob.uchicago.edu

## ABSTRACT

The very weak polarization of light from nearby stars reaches a maximum near the ecliptic plane in a position offset by  $\lambda \sim 35^\circ$  from the heliosphere nose direction. The position angle for the polarization in this ecliptic-plane peak is the same for near and distant stars, to within uncertainties, indicating the interstellar magnetic field direction is relatively constant over several hundred parsecs in this region. This region is near the center of a magnetic bubble that has recently been identified by Wolleben. The magnetic field directions defined by the polarizations of nearby and distant stars in the direction of this polarization maximum, and also by the observed offset between interstellar He $^{\circ}$  and H $^{\circ}$  flowing into the heliosphere, converge to a local magnetic field direction that is inclined by  $\sim 55^\circ$  with respect to the galactic plane, or  $\sim 65^\circ$  with respect to the ecliptic plane. Surprisingly, the geometry of the cosmic microwave background (CMB) dipole moment shows a strong correlation with this heliosphere geometry. Several vectors associated with the CMB low- $\ell$  multipole moments are located at the positions of heliosphere landmarks such as the 3 kHz emissions detected by the Voyager 1 and Voyager 2 satellites. Together these results suggest that an unrecognized heliospheric foreground is present in the measured CMB background. All data are consistent with the expansion of the S1 subshell of the Loop I magnetic bubble to the solar location. The magnetic field in this shell then determines the field direction at the Sun, helps shape the heliosphere, and generates an additional unrecognized CMB foreground.

*Subject headings:* ISM: magnetic fields, dust, heliosphere— cosmology: miscellaneous— solar system: general

## 1. Introduction

Interstellar dust grains location are a potential diagnostic of the interaction between the solar wind and the interstellar medium. The relative velocity between the Sun and the surrounding interstellar cloud is  $26.3 \text{ km s}^{-1}$ , and neutral interstellar gas and large dust grains flow through the raindrop-shaped solar wind bubble known as the heliosphere. Interstellar ions and the small interstellar dust grains that dominate interstellar polarization are trapped in the interstellar magnetic field that is deflected around the heliosphere.

The fundamental interstellar properties that dominate the shape of the heliosphere are the direction and strength of the magnetic field  $B_{\text{IS}}$ , the ionization level, and the thermal and ram pressure of gas (e.g. Holzer 1989). The upstream directions of interstellar  $\text{H}^\circ$  and  $\text{He}^\circ$  inside the heliosphere differ by  $5^\circ$ , serving as a diagnostic of the interstellar magnetic field at the Sun (Weller & Meier 1974; Quémerais et al. 2000; Lallement et al. 2005). A second diagnostic of  $B_{\text{IS}}$  at the heliosphere is the polarization of light from nearby stars in the galactic center hemisphere, discovered by (Tinbergen 1982, T82) and now interpreted as partly caused by interstellar dust grains trapped in the outer heliosphere regions (Frisch 2005, Paper I). The polarization maximum occurs for stars near the ecliptic plane and located at ecliptic longitudes of about  $\sim +35^\circ$  from the upstream directions given by interstellar dust and  $\text{He}^\circ$ .

Three independent sets of data indicate that the heliosphere shape is not symmetric around the upwind direction of interstellar material (ISM) flowing into the heliosphere. Voyager 1 crossed the solar wind termination shock (TS) at 94 AU in December 2004, and Voyager 2 crossed the TS at  $\sim 84$  AU in August 2007, indicating the TS is closer by  $\sim 10$  AU in the southern ecliptic compared to northern ecliptic regions (Stone 2007; Stone et al. 2005; Burlaga et al. 2005; Decker et al. 2005). These asymmetries result from an interstellar magnetic field inclined to the velocity of inflowing ISM (Pogorelov et al. 2004; Opher et al. 2007). Observations of low frequency radio emissions (1.8–3.6 kHz) by the plasma wave instruments on Voyager 1 and 2 during 1992–1994 showed that these events arise  $\sim 130$  AU from the Sun at the edge of the heliosphere, and that the events are consistent with an asymmetric heliosphere (Kurth & Gurnett 2003; Gurnett et al. 2006, Appendix B). The third data set consists of measurements of  $\sim 1$  keV energetic neutral atoms (ENAs) near the heliosphere nose, that have an origin offset to positive ecliptic longitudes compared to the heliosphere nose direction of  $\lambda \sim 10^\circ - 40^\circ$  (Collier et al. 2004; Wurz et al. 2004). ENAs are formed beyond the termination shock by charge exchange between interstellar  $\text{H}^\circ$  and the solar wind; the ENAs show the bulges in the solar wind such as the heliotail and the neutral current sheet wrapping around the heliosphere nose (Heerikhuisen et al. 2007).

The asymmetry of the outer heliosphere may vary with time since the solar magnetic

activity cycle causes the solar and interstellar magnetic field lines to alternate between parallel and antiparallel modes (e.g. Nerney et al. 1995; Macek 1990; Washimi & Tanaka 1996; Zurbuchen 2007). The Tinbergen polarization data and 3 kHz data were collected during north-pole-positive polarities, with field lines emerging at the solar north pole. The Voyager satellites crossing of the termination shock occurred during solar cycle phases when the south pole had a positive polarity.

The structure of this paper is as follows. The polarization data that yield the local magnetic field direction are discussed in §2.1, with more details in Appendix A.. The polarization data used in Paper I are augmented with additional data acquired during the 1970’s. The question as to whether this weak polarization originates at the Sun or in nearby ISM in the upwind direction is discussed in §2.2. The magnetic field direction of nearby and distant stars in the ecliptic nose region for near and far stars are found to be similar (§3.1), and yield a magnetic field direction at the Sun that is independent of whether the polarization is formed at the heliosphere or in the nearest upwind ISM (§3). Several characteristics of the low- $\ell$  components of the cosmic microwave background that are related to the heliosphere are discussed in §4, including the area vectors that occur in the direction of the 3 kHz emissions, the relation of the hot and cold poles of the CMB Doppler dipole to the heliosphere, and the distribution of nearby ISM. The influence on the local magnetic field direction of the S1 magnetic bubble is discussed in §5. Conclusions are presented in §6. Appendix A presents additional details about the optical polarization data, and discusses the coincidental correlation between the position angles of distant stars and ecliptic latitude. Appendix B briefly discusses primary versus alternate locations found for the 3 kHz emissions observed by the Voyager satellites.

The conclusions in the following discussions are sensitive to the physical properties of the ISM surrounding the Sun. The ISM at the solar location has a temperature of  $6300 \pm 340$  K, a heliocentric velocity of  $-26.3 \text{ km s}^{-1}$ , and an upstream direction near the ecliptic plane at  $\lambda = 254.7 \pm 0.5^\circ$ ,  $\beta = 5.1 \pm 0.2^\circ$  (corresponding to  $\ell = 3.5^\circ$ ,  $b = 15.2^\circ$ ), based on Ulysses interstellar  $\text{He}^\circ$  data (Möbius et al. 2004; Witte 2004, W04). The ISM flow through the heliosphere contains dust grains, which are observed at the same velocity and flow direction as the gas (Grün et al. 1993; Baguhl et al. 1996; Grün et al. 2005; Frisch et al. 1999). The dust-to-gas mass ratio for the ISM flowing into the heliosphere is  $< 120$ , compared to  $> 180$  for the LIC (SF07). Models that evaluate the ionization gradient in the surrounding ISM yield interstellar  $\text{H}^\circ$  densities at the Sun of  $n(\text{H}^\circ) = 0.19 \text{ cm}^{-3}$ , and electron densities  $n(e) = 0.07 \pm 0.01 \text{ cm}^{-3}$  (e.g. Model 26 in Slavin & Frisch 2007, SF07). The plasma oscillation frequency of ISM at the Sun is then  $\sim 2.4 \text{ kHz}$ , but will rise to higher values in the interstellar plasma pile-up in the outer heliosheath. If the partially ionized gas close to the Sun is in pressure equilibrium with  $B_{\text{IS}}$ , then  $P_{\text{B}} \sim P_{\text{th}} \sim 0.2 \text{ eV}$  and  $B_{\text{IS}} \sim 2.8 \mu\text{G}$ . If the gas and interstellar magnetic

field are in pressure equilibrium the heliosphere has a Mach $\sim 1$  bowshock.

## 2. Local Magnetic Field Direction from Interstellar Polarization Data

The direction of the interstellar magnetic field at the Sun is measured from starlight polarization. Weak but systematic polarization of light from stars within 40 pc in a region in the galactic center hemisphere was discovered by Tinbergen (1982). Tinbergen attributed this weak polarization, where detections are at the  $3\sigma - 5\sigma$  level, to a patch of ISM close to the Sun. Tinbergen’s data were acquired during solar minimum conditions, in the south during 1974 and in the north during 1973 (J. Tinbergen, private communication). <sup>1</sup> Paper I showed that this polarization reaches a maximum at a location offset by  $\sim +35^\circ$  from the heliosphere nose. Below it is shown that this maximum also occurs in the ecliptic plane, and that the weak polarizations extend to negative ecliptic latitudes in the eastern hemisphere of the heliosphere (§2.1). The weak polarization observed by Tinbergen appears to arise from interstellar dust interacting with the heliosphere (§2.2.1). Data are sparse and additional observations are needed.

### 2.1. Polarization Data for Nearby Stars

The catalog of polarizations of nearby stars used here consists of data from Tinbergen (1982) and Piirola (1977, acquired in 1974). This combined Tinbergen-Piirola catalog (TPC) has 202 stars, 86% of which are within 40 pc (for Hipparcos distances). The two data sets have 45 stars in common; the noisiest data from the original studies are omitted from this discussion. The errors on the mean Stokes parameters are discussed by Tinbergen, and are  $6 - 17 \times 10^{-5}$ ; combining different measurements yielded  $1\sigma \sim 6 \times 10^{-5}$  (Table 1 of Tinbergen 1982). The unit  $P_5 = 10^{-5}$  degree of polarization will be used. The linear Stokes parameters U and Q give polarization  $P = (Q^2 + U^2)^{1/2}$ .

The polarizations of the TPC are plotted in Fig. 1 in an Aitoff projection. A region within  $30^\circ$  of the ecliptic meridian  $\lambda \sim 280^\circ$  shows the strongest polarizations down to latitudes of  $\beta \sim -45^\circ$ . The polarization for stars close to the ecliptic plane reaches a maximum at a location offset by  $\Delta\lambda \sim +35^\circ$  from the heliosphere nose.

The average polarization as a function of  $\lambda$  is plotted in Fig. 2, with averages smoothed

---

<sup>1</sup>During the mid-1970’s, the solar magnetic polarity was north pole positive ( $A > 0$ , field lines emerging at the north pole).

over  $\pm 20^\circ$  around the central ecliptic longitude  $\lambda_0$  because of the small number of stars. Averages are shown for stars within  $20^\circ$ , and within  $50^\circ$ , of the ecliptic plane. The polarization peaks at  $\lambda \sim 295^\circ$  for stars with  $|\beta| < 20^\circ$ . The polarization peak is offset by  $\sim +30^\circ$  and  $\sim +40^\circ$  from the upwind directions of interstellar dust and  $\text{He}^\circ$ , respectively. The uncertainties on the polarization data have been carefully discussed by Tinbergen (1982) and Piirola (1977). Paper I used only the Tinbergen (1982) data; the addition here of the Piirola (1977) data improves the statistics for many regions of the sky, but not in the heliosphere nose direction. Additional information on the smoothing process is given in Appendix A. These polarizations are weak,  $\sim 0.02\%$ , and have been detected at the  $3\sigma - 5\sigma$  levels. The polarization maximum regions coincides with upstream direction of the ENA flux observed from the outer heliosphere (§2.2.1). Fig. 1 also shows the upstream direction of dust grains flowing into the heliosphere (from Ulysses and Galileo data, Frisch et al. 1999) and of interstellar  $\text{He}^\circ$  flowing into the heliosphere (Witte 2004; Möbius et al. 2004).

The weak polarization becomes unobservable when the angle between the sightline and the direction of the magnetic field,  $\hat{k}_B$ , deviates significantly from  $90^\circ$ . This condition can be estimated because the observed polarization can not be identified when  $P < 2.5\sigma$ , so the polarization is only detected in stars within  $\sim 40^\circ$  of the perpendicular direction to  $B_{\text{IS}}$ .

## 2.2. Is Polarization Origin at Heliosphere or in Nearby Upwind ISM?

### 2.2.1. Polarization Origin at Heliosphere

Several characteristics support the origin of this weak polarization in the outer heliosheath region (defined as the region between the heliopause and bow shock). The first is that the upwind polarizations are strongest in the ecliptic plane (§2.1). The five stars that dominate the upstream polarization maximum in the ecliptic plane have the same polarization position angles (§3.1, Table 1, Appendix A). The polarization maximum region is elongated along the ecliptic plane towards positive longitudes. This may indicate either a blunt heliosphere or the sideways deflection of the grains following  $B_{\text{IS}}$  around the heliosphere.

The second argument supporting an outer heliosheath origin of the polarization is that the small grains capable of polarizing starlight are tied by small gyroradii to the interstellar magnetic field deflected around the heliosphere. The magnetic field upstream of the heliopause filters out grains with large charge-to-mass ratios,  $Q/M$ , and gyroradii that are smaller than the characteristic lengths between the heliosphere bow shock and heliopause (e.g., Frisch et al. 1999; Czechowski & Mann 2003; Linde & Gombosi 2000). Dust grains in

the LIC are silicates (SF07). The radii of the magnetically excluded grains are  $\lesssim 0.1 - 0.25 \mu\text{G}$ , and are comparable to the sizes of interstellar polarizing grains (e.g. Mathis 1986).

The coincidence of the polarization maximum location with the ENA flux from the outer heliosphere (Collier et al. 2004; Wurz et al. 2004) may indicate that maximum charge densities in the outer heliosheath occur where the strongest compression of the interstellar magnetic field occurs. The photoejection of electrons gives positively charged dust grains (Weingartner 2004), and ENAs form where interstellar neutrals charge exchange with protons, indicating ENAs and small dust grains in the outer heliosheath may have similar distributions. The properties of the outer heliosheath regions are not yet understood, and IBEX data on ENAs will elucidate the processes of the outer heliosphere (McComas et al. 2005).

The polarization increases by  $\sim 46\%$  between the  $3\sigma$  detection towards 36 Oph AB at 6 pc, and HD 161892 at 39 pc and  $5^\circ$  away from 36 Oph AB. This suggests the observed polarization is partly formed beyond the heliosphere in the cloud, but that the polarization level is boosted to detectable levels in the ecliptic plane where the interstellar magnetic field is compressed between the bow shock and heliopause and grain charging rates differ from those in the ISM.

Interstellar dust grains traversing the outer heliosheath experience a gradient in magnetic field direction and strength, plasma density, and grain charging rates, so that the grain gyroradii vary with position. Czechowski & Mann (2003) have modeled the passage of interstellar dust grains across the transition region between the ISM and the heliopause and found that in the presence of a strong shock small grains develop velocity differences compared to the plasma velocity, and are deflected to the heliosphere flanks. Such a process may explain the  $\sim 35^\circ$  offset in the polarization maximum from the upstream direction. For some magnetic field directions and grain masses, grains are reflected back away from the heliopause and form density waves. The following section shows that collisional disruption of grain alignment is slow. This indicates that polarization position angles will not vary if the  $B_{\text{IS}}$  component in the plane of the sky is relatively constant as the field is initially displaced by the heliosphere.

The polarizations appear to be strong for the small ( $\sim 150$  AU) distance between the heliopause and bow shock. Comparisons between 36 Oph AB and HD 161892 suggests that only half of the polarization must originate in the outer heliosheath to boost the polarization strength to detectable levels (§2.1). There are no comparable data sets of high-sensitivity very weak optical polarizations with which to compare the Tinbergen data.

### 2.2.2. Polarization Origin in Upwind ISM

The Sun is located in an interstellar cloud that is part of a decelerating cluster of local interstellar cloudlets (CLIC) flowing away from the direction of the Scorpius-Centaurus Association and past the Sun (Frisch 1995; Frisch et al. 2002). Figure 3 shows the distribution of neutral ISM within 15 pc for sightlines with  $N(\text{H}^\circ) > 1.0 \times 10^{18} \text{ cm}^{-2}$ , based on data in Wood et al. (2005) and Redfield & Linsky (2004), and for some stars using the assumption  $\text{D}^\circ/\text{H}^\circ = 1.5 \times 10^{-5}$ . Interstellar  $\text{H}^\circ$  within 15 pc is seen to coincide with the eastern hemisphere of the heliosphere. The initial interpretation of the Tinbergen data was that the polarizations were formed in this nearby patch of ISM in the galactic center hemisphere (T82; Frisch & York 1983; Bruhweiler 1984). Comparisons between the polarizations of 36 Oph AB and HD 161892 suggest that the starlight polarization observed in the ecliptic plane maximum also includes a contribution from ISM upstream of the heliosphere nose (§2.1). This ISM within 15 pc appears to be the closest part of a magnetic shell from Loop I that has expanded to the solar location (see §5).

The polarization maximum in the ecliptic plane is seen to occur in a sightline through the boundary of the ISM within 15 pc. The possibility that the CLIC is the exclusive origin of the upwind polarizations concentrated in the ecliptic plane can not be ruled out. Most of the polarization is formed near the ecliptic meridian  $\lambda \sim 280^\circ$ , which cuts through the low column density boundary of the ISM shown in Fig. 3. Ionization levels and magnetic field strengths may be higher towards the boundary regions than in the cloud interior, yielding stronger polarizations. Stars in the CLIC that are located between  $\lambda \sim 330^\circ$  and  $\lambda \sim 60^\circ$  are unpolarized. For stars towards the polarization maximum near the ecliptic plane, polarization position angles from interstellar dust grains in the outer heliosheath and from grains in the upstream ISM should be the same, since polarization position angles do not change significantly over the nearest  $\sim 200$  pc in this direction (§3.2),

Grain alignment persists over long time scales in low density gas such as is upwind of the Sun, when compared to the denser clouds. Low densities significantly reduce the collisional disalignment of the dust grains when compared to denser clouds. The minimum and maximum mean densities for the  $\text{H}^\circ$  within 15 pc are  $\langle n(\text{H}^\circ) \rangle = 0.01 \text{ cm}^{-3}$  and  $0.12 \text{ cm}^{-3}$ , respectively, and the average density for stars within 15 pc is  $0.05 \text{ atoms cm}^{-3}$ . The LIC is less dense by a factor of  $\sim 65$ , warmer by a factor of  $\sim 100$ , with proton densities a factor of  $\sim 10$  larger than typical cold ISM. Grain alignment is disrupted when grains accumulate their own mass in thermal collisions with the gas, which occurs over time scales of  $\tau_{\text{mass}} \sim 10^6 a \rho_{\text{gr}} / n \sqrt{T_{\text{gas}}} \text{ Myrs} = 0.7\text{--}1.2 \text{ Myrs}$  in the LIC. In the LIC the collision rate is down by a factor of  $\sim n / \sqrt{T} \sim 600$  compared to denser clouds, so that even though  $B_{\text{IS}}$  is weaker in the LIC compared to dense clouds, it is fundamentally easier to magnetically align

ISDGs in the LIC than in denser clouds. Although precise spatial densities are not known for the upwind ISM, the low average densities indicate similar arguments will apply.

### 3. Magnetic Field Direction at Polarization Maximum in Ecliptic Plane

The direction of the local interstellar magnetic field is established by polarization position angles of starlight. The magnetic field direction towards the polarization maximum in the ecliptic plane is the same for local stars (§3.1) and distant stars in the same region (§3.2). The polarization position angle in celestial coordinates of the plane of vibration of the electric vector is given by  $\theta_C = 0.5 \arctan(U/Q)$  (also see Appendix A). The interstellar magnetic field is parallel to the polarization, as is shown by synchrotron emission that is polarized perpendicular to the field direction (e.g. Heiles 1976).

#### 3.1. Magnetic Field Direction near the Sun

The stars in the polarization maximum near the heliosphere nose have a mean position angle in ecliptic coordinates of  $PA_E = -25^\circ \pm 4^\circ$  (Table 1). The polarization position angles do not vary significantly with ecliptic longitude in the polarization maximum region (see Appendix A). The interstellar magnetic field direction is parallel to the polarization vector (Spitzer 1978). The polarization position angles indicate that the magnetic field direction close to the Sun is inclined by  $\sim 55^\circ$  with respect to the galactic plane and  $\sim 65^\circ$  with respect to the ecliptic plane, regardless of whether the polarization originates in the outer heliosheath or in the very local ISM.

The  $5^\circ$  angular offset between the interstellar  $He^o$  and  $H^o$  flowing through the heliosphere, discovered by Weller & Meier (1974) and now accurately determined using Ulysses  $He^o$  data and SOHO  $H^o$  Ly $\alpha$  fluorescence data, is also a diagnostic of the interstellar magnetic field direction at the Sun (Witte 2004; Quémerais et al. 2000; Lallement et al. 2005). The  $H^o$  and  $He^o$  upstream directions (Table 2) can be used to define a position angle for comparison with the polarization data. This position angle is the  $H^o$  upwind direction with respect to a great circle meridian passing through the  $He^o$  upwind direction, and is  $PA_{E, HHe} = -33^\circ \pm 14^\circ$  in ecliptic coordinates (Table 1). The magnetic field directions defined by starlight polarization in the heliosphere nose, and by the  $5^\circ$  offset between  $H^o$  and  $He^o$  flowing into the heliosphere, therefore give the same result to within the uncertainties. However a component of the magnetic field that is parallel to the sightline would not be detected by these methods.



### 3.2. Magnetic Field Direction from Distant Stars

The upwind direction of the LIC corresponds to an astronomically interesting direction, dominated by the North Polar Spur (Frisch 1981), which is the radio-intense section of the Loop I superbubble shell that is traced by both polarized synchrotron emission and magnetically aligned dust grains (e.g. Heiles 1976). As a test of the relation between the nearby and distant magnetic field in the direction of the heliosphere nose, the polarization position angles for stars in the TPC are compared with those of distant stars in the Heiles Polarization Catalog (HPC, Heiles 2000, available on Vizier as catalog II/226). The scaled polarizations for stars 40–100 pc distant and within  $20^\circ$  of the ecliptic plane are plotted versus  $\lambda$  in Fig. 2, where the polarizations are smoothed over ecliptic intervals of  $\pm 5^\circ$  from the central longitude. Locations where the ecliptic crosses Loop I are seen as two polarization peaks at  $\lambda \sim 264^\circ$  and  $\lambda \sim 220^\circ$ , and the strongest peak near  $\ell \sim 4^\circ$  and  $b \sim 4^\circ$  is within  $10^\circ$  of the ecliptic nose direction.

The polarizations of stars in the HPC within 250 pc are displayed in Fig. 5, using only objects with HD numbers and parallaxes in the Hipparcos catalog (Perryman 1997). No screening is made for discrepancies between the celestial and galactic positional angles listed in the HPC. The familiar pattern of magnetic filaments traced by polarization vectors is evident.

The comparison between the position angles of near and far stars in the heliosphere nose region of maximum polarization has two distinct properties. First, for stars in the heliosphere nose region the average position angle of the distant stars in the HPC is  $\text{PA}_E = -20^\circ \pm 20^\circ$ , in agreement with the TPC data (Table 1, Fig. 5). Slightly different definitions of the heliosphere nose region are used for the TPC versus the HPC stars because of the small number of TPC stars (see Table 1 for region specifications). These position angles for the nearby TPC stars agree to within uncertainties with those of the distant HPC stars in the region of maximum nearby polarization. For example, the nearby star HD 155885 (6 pc) and distant star HD 157236 (189 pc) in the same direction towards the heliosphere nose both have the same polarization position angle ( $\text{PA}_G = 39^\circ$  in galactic coordinates), although the polarization of HD 157236 is stronger than for HD 155885. Second, for a more extended spatial interval around the heliosphere nose the position angles of the distant stars vary systematically with *ecliptic* latitude, due to the chance alignment of a Loop I magnetic filament (this is shown in Appendix A).

Close to the ecliptic plane in the polarization maximum region the distant and nearby stars show the same mean polarization position angles. The similarity in the polarization position angles of nearby stars within 40 pc, and distant stars (140–240 pc) that trace the Loop I magnetic field, indicates that the interstellar magnetic field is well-ordered over sev-

eral hundred parsecs in this direction, and interstellar densities are low, minimizing the collisional disruption of the aligned grains. It is surprising that the polarization data indicate the interstellar magnetic is well-ordered over a few hundred parsecs, especially since the distant region includes the Riegel-Crutcher cold cloud where magnetic filaments are seen (Riegel & Crutcher 1972; McClure-Griffiths et al. 2006). However the Local Bubble surroundings of the Sun provide a minimal barrier to the expansion of Loop I (Frisch 1981). Superbubbles formed by stellar evolution in the Sco-Cen Association during the past  $\sim 5$  Myrs evidently dominate morphology of the local interstellar magnetic field.

#### 4. Evidence for Unrecognized Foreground Contamination of the Cosmic Microwave Background

Paper I suggested that the interstellar dust grains trapped in the outer heliosheath and deflected around the heliosphere may contribute a weak unrecognized foreground to the cosmic microwave background. The large scale CMB power spectrum contains poorly understood anomalies related to ecliptic geometry, indicating that the low- $\ell$  CMB may have unrecognized very local foreground contamination related to the ecliptic geometry (e.g. Eriksen et al. 2004; Schwarz et al. 2004). These anomalies appear in the Year 1, and remain in the Years 1-3 WMAP data after instrumental corrections were improved (Hinshaw et al. 2007a; Copi et al. 2007). The interstellar magnetic field near the Sun (§3) and small interstellar dust grains excluded from the heliosphere (§2.1) both provide possible foreground contaminants of the CMB radiation.

In this section the geometrical properties of the CMB low- $\ell$  moments are compared to the geometrical properties of heliospheric phenomena. Several coincidences are found. The geometrical properties of what has been identified as the Doppler contribution to the CMB dipole moment (e.g. Mather et al. 1994) are related to both the heliosphere geometry and the distribution of ISM within 35 pc. CMB low- $\ell$  multipole moments, including the non-cosmological Doppler shift to the CMB dipole moment, and the quadrupole and octopole multipoles, trace important heliospheric quantities. The interstellar magnetic field at the Sun may influence these apparently independent phenomena, and this field direction appears to be determined by the S1 subshell of Loop I (§5).

This qualitative discussion focuses on the spatial coincidences between the CMB and heliosphere properties. The source of possible heliospheric contamination of the CMB microwave radiation is unknown. The outer heliosphere region is only recently explored for the first time by Voyager 1 and Voyager 2, which have crossed the solar wind termination shock at 94 AU and 85 AU in December 2004 and August 2007, respectively. Since the heliosphere

itself varies with the magnetic solar cycle of the Sun, any possible heliospheric foreground to the CMB radiation may vary with solar cycle phase.

#### 4.1. CMB Features Related to Heliosphere and Local ISM

Figures 6 and Fig. 7 summarize the geometrical coincidences between the CMB low- $\ell$  multipole moments and heliospheric properties.

Structure in the Cosmic Microwave Background (CMB) signal over large angular scales was detected in the COBE maps (Smoot et al. 1992; Kogut et al. 1992; Mather et al. 1994), and persists in the high signal-to-noise Wilkinson Microwave Analyzer Polarimeter (WMAP) data (e.g. Bennett et al. 2003; Hinshaw et al. 2007a). The anisotropies of the CMB at large angular scales are dominated by characteristic anisotropies which include a dipole moment of amplitude  $\Delta T/T \sim 10^{-3}$  due to the energy shift induced by the Doppler motion through the CMB rest frame, a weaker quadrupole moment with amplitude  $\Delta T/T \sim 10^{-5.2}$ , and weak higher order asymmetries (Smoot et al. 1977, 1992; Kogut et al. 1993).

The plane that separates the hot and cold hemispheres of the CMB dipole moment traverses the heliosphere nose  $\sim 6^\circ$  from the upstream direction defined by interstellar  $\text{He}^\circ$  flowing into the heliosphere (Table 2). The poles of the CMB Doppler motion are therefore nearly equidistant from the inflow direction of ISM into the heliosphere, and the plane separating the hot and cold hemispheres of the CMB dipole moment separates the eastern and western parts of the heliosphere (Fig. 6).<sup>2</sup> The position angle defined by this plane, at the point of closest approach to the heliosphere nose, is within  $15^\circ$  of the position angles of the polarizations in the ecliptic plane maximum (Table 1).<sup>3</sup> The plane separating the hot and cold hemispheres of the CMB dipole moment therefore appears to be within  $\sim 15^\circ$  of the interstellar magnetic field direction at the Sun found from optical polarizations. For comparison, the WMAP ILC3 map data (Hinshaw et al. 2007a) are plotted in Fig. 7 in ecliptic coordinates, with the same features as shown as in Fig. 6.

Anomalies also appear in the low- $\ell$  quadrupole and octopole moments. Using “multipole vectors” to decompose the Internal Linear Combination map, Years 1-3 (ILC3) data, Copi

---

<sup>2</sup>This fact does not appear to have been discussed previously in the literature. Smoot et al. (1977) report that Peebles referred to the CMB kinematic Doppler dipole as the “new aether drift”.

<sup>3</sup>By coincidence the heliocentric upstream direction of ISM flowing through the heliosphere, which represents the vector sum of the solar and LIC motions through the LSR, is within  $\sim 5^\circ$  of the ecliptic plane and  $\sim 15^\circ$  of the galactic center.

et al. (2007) found that there is an alignment between the quadrupole and octopole planes, and that the ecliptic traces a zero between the extremes in the quadrupole and octopole moments. The multipole vectors carry the angular distribution information of the power for each  $\ell$ -value. Copi et al. showed that the  $\vec{w}$  area vectors (normals to planes defined by multipole pairs) coincide with the ecliptic plane for southern galactic latitudes. In Fig. 6 the positions of the  $\ell=2$  and 3 multipole vectors  $\hat{v}$ , and  $\vec{w}$  area vectors, are plotted in ecliptic coordinates (locations from Copi et al. 2007, Table 1, ILC123 data). The  $v^{22}$  component is directed towards the heliosphere nose. The four area vectors  $w^{323}$ ,  $w^{212}$ ,  $w^{312}$ , and  $w^{331}$  are all directed towards or close to the strip on the sky containing the 3 kHz emissions (Appendix B) and the hot pole of the dipole. This strip is nearly perpendicular to the ecliptic plane, in the sidewind direction corresponding to ecliptic longitude  $\lambda \sim 180^\circ$  (Fig. 1). The 3 kHz emissions are formed where outward propagating global merged interaction regions interact with the magnetically-shaped heliopause (Mitchell et al. 2004). The low- $\ell$  moments of the CMB therefore appear to respond to the ecliptic coordinate system partly because of the shaping of the heliosphere by the interstellar magnetic field.

Separate analysis of the WMAP data as a function of solar cycle phase may yield clues about the origin of the new foreground. Copi et al. (2007) pointed out that there is a discrepancy between the Year 1 and Year 1–3 quadrupole moments. WMAP was launched in June 2001, and the Year 1 data represent data acquired between Sept. 2001 and Sept. 2002 during solar maximum conditions, versus between Sept. 2001 and Sept. 2004 for the Year 1–3 period that includes the solar minimum conditions of 2004. The shift of the  $v^{22}$  multipole from  $\lambda=268.9^\circ$ ,  $\beta=15.6^\circ$  during Year 1 (17.6° away from the upwind direction) to  $\lambda=252.6^\circ$ ,  $\beta=8.2^\circ$  during Years 1–3 (3.7° from the upwind direction) indicates that the process contributing CMB foreground may be solar cycle dependent. An analogous shift has not been reported for the upstream direction of inflowing  $\text{He}^0$ , which has been measured up to 2003 by Ulysses (Witte 2004; Möbius et al. 2004).

#### 4.2. The CMB Dipole Moment and Local Interstellar Matter

The cold hemisphere of the CMB dipole moment coincides with the location of neutral ISM within 15 pc with  $N(\text{H}^0) > 10^{-18} \text{ cm}^{-2}$  (Fig. 3). When the highest column densities of interstellar  $\text{H}^0$  within 35 pc are plotted, the hot pole of the CMB dipole moment is seen to coincide with distant parts of the S1 magnetic shell (Fig. 4, §5). Together with the polarization data, this indicates that the S1 magnetic bubble has expanded to the solar location. CMB foreground templates calculated for synchrotron emissivity do not include contributions from a local magnetic field or this magnetic bubble.

## 5. S1 Subshell of Loop I Superbubble as Explanation of Local Magnetic Field

The relation between the ISM at the Sun and the Loop I superbubble formed by stellar evolution in the Scorpius-Centaurus Association was discovered from the kinematics and abundances seen in ISM upwind of the Sun (Frisch 1981), and has now been investigated in a number of studies (e.g. Crutcher 1982; Bochkarev 1984; Crawford 1991; de Geus 1992; Frisch 1995; Breitschwerdt et al. 2000; Maíz-Apellániz 2001). Recently the Loop I magnetic superbubble has been modeled as the superposition of two magnetic bubbles with centers offset from each other by  $\sim 37^\circ$  (Wolleben 2007). The nearest of these structures, S1, is centered at  $\ell = 346^\circ \pm 5^\circ$ ,  $b = 3^\circ \pm 5^\circ$ , distance  $68 \pm 10$  pc, with radii for the inner and outer rims of  $72 \pm 10$  pc and  $91 \pm 10$  pc, respectively. The inner and outer tangential rims of S1 are approximated as circles and plotted in ecliptic coordinates in Figs. 3 and 4, and in galactic coordinates in Fig. 5. The nearest CLIC gas,  $d < 15$  pc, coincides roughly with the eastern part of the S1 shell (Fig. 3). Interstellar  $\text{H}^\circ$  with  $N(\text{H}^\circ) > 2 \times 10^{-18}$  traces the tangential regions through the western part of the shell (Fig. 4). The upwind direction of the CLIC in the local standard of rest is centered near the center of the S1 shell. The best fit bulk flow velocity of interstellar cloudlets within 30 pc is  $-17 \text{ km s}^{-1}$  from  $\ell, b = 0^\circ, -5^\circ$  (Frisch et al. 2002), using the Hipparcos solar apex motion (Dehnen & Binney 1998).

The CLIC  $\text{H}^\circ$  densities decrease towards the shell center as if the CLIC is part of the expanding shell. The  $\text{H}^\circ$  minimum is centered near  $\ell \sim 330^\circ$  and  $b \sim +8^\circ$ , where the radiation field from hot stars from the Upper Centaurus Lupus subgroup of the Centaurus association appears to ionized upwind CLIC gas in the solar vicinity. An additional source of ionizing radiation is the white dwarf star WD1634-573, located at  $\ell = 330^\circ$ ,  $b = -7^\circ$ , and where 60% of the gas is ionized (Wood et al. 2002).

The locations of the two poles of the CMB dipole moment both fall just outside of the S1 shell, and coincide with the  $\text{H}^\circ$  gas surrounding the S1 magnetic shell (Fig. 4).

Partially ionized ISM is tied to the interstellar magnetic field so that gas and dust are trapped in the expanding S1 magnetic shell. If the LIC gas and magnetic field at the Sun are in pressure equilibrium, then  $|B_{\text{IS}}| \sim 2.8 \mu\text{G}$  (Model 26, SF07). For the warm LIC,  $T > 5000$  K, the proton gyroradius is  $< 0.4$  pc and the ISM will couple to the magnetic field in the moving shell unless cloud densities are  $n(\text{H}^\circ) > 2 \text{ cm}^{-3}$  (which is possible but not likely, Frisch 2003). However there is a well-known discontinuity in the velocity of the LIC versus the upstream gas towards the nearest star  $\alpha$  Cen (e.g. Linsky & Wood 1996; Landsman et al. 1984), indicating possible substructure in the S1 shell induced by higher field strengths. The position angle data indicate that the magnetic field direction does not vary significantly over several hundred parsecs in the upstream direction in the region of the ecliptic-plane-polarization-maximum, so there must be empty regions of space with minimal

dust between the near and far fields, such as expected for the interior of a magnetic bubble.

Rotation measures of pulsars and extragalactic radio sources show that the uniform component of the interstellar magnetic field in the interarm region around Sun is directed towards  $\ell \sim 82^\circ$ . The strength of the large-scale galactic regular magnetic field at the solar radius is  $B_{\text{IS}} \sim 2.1 \pm 0.3 \mu\text{G}$ , found from rotation and dispersion measures towards an assembly of pulsars within several kiloparsecs of the Sun (Han 2006). Faraday rotation data show that the large-scale magnetic field reverses polarity around the galactic  $\ell=0^\circ$  meridian at the galactic center and also around the galactic plane. In the part of the CLIC within 15 pc,  $b < 0^\circ$  and  $\lambda > 270^\circ$ , the global field polarity is directed away from the Sun.

The polarization data establish the direction of the magnetic field at the Sun (Table 1). Radio synchrotron polarization data indicate that the optical polarization vector is parallel to the magnetic field direction in the Loop I filament, and there is no reason to assume otherwise for the local ISM, especially given the coincidence in position angles for near and far polarization. However, there may be a component of  $B_{\text{IS}}$  that is perpendicular to the plane of the sky that is not sampled by optical polarization. For a high-latitude direction through the distant Loop I, the  $B_{\text{IS}}$  component parallel to the sightline is small. At the location  $\ell = 34^\circ$ ,  $b = 42^\circ$ , where a  $\sim 70 \pm 30$  pc tangential sightline through Loop I is sampled, the volume-averaged field strength is  $B_{\text{IS}} \sim 4 \mu\text{G}$  (Heiles et al. 1980). For this sightline, the Faraday rotation of extragalactic radio sources indicate the  $B_{\text{IS}}$  component parallel to the sightline is small, with an average value of  $B_{\parallel} = 0.9 \pm 0.3 \mu\text{G}$  (Frick et al. 2001).

## 6. Conclusions

- The polarizations of nearby stars,  $< 45$  pc, form a maximum in the ecliptic plane that peaks at an ecliptic longitude shifted by  $\sim 35^\circ$  from the upstream direction of interstellar gas and dust flowing into the heliosphere. Half of this polarization is formed within  $\sim 6$  pc of the Sun, and the polarization maximum indicates a significant contribution from small interstellar dust grains interacting with the outer heliosheath regions.
- The polarization position angles of nearby and distant stars in this polarization peak agree to within the uncertainties (Table 1). The position angle defined by the offset between the upstream directions of interstellar  $\text{He}^\circ$  and  $\text{H}^\circ$  in the heliosphere also agrees with the position angles found from the polarization-peak stars, to within the uncertainties.
- These polarization data give a direction for the interstellar magnetic field at the Sun

that is inclined by  $\sim 65^\circ$  with respect to the ecliptic plane, and  $\sim 55^\circ$  with respect to the galactic plane. An additional component into the plane of the sky may also be present. If the interstellar magnetic field direction nearby is similar to the global field in the solar vicinity, then the field is directed away from the Sun east of the heliosphere nose in ecliptic coordinates.

- The plane that separates the cold and hot hemispheres of the CMB dipole moment also divides the east and west hemispheres of the heliosphere, and also encloses most sightlines within 15 pc that have interstellar  $N(\text{H}^\circ) > 1.0 \times 10^{18} \text{ cm}^{-2}$ .
- The CMB quadrupole area vectors of Copi et al. (2007) line up with the positions of the locations of the 3 kHz events detected by Voyagers 1 and 2. A mix of primary and alternate locations for the 3 kHz emissions are used for this comparison (Appendix B).
- A plane can be formed from points that are equidistant between the two poles of the CMB dipole. At the closest point to the heliosphere nose direction defined by inflowing interstellar  $\text{He}^\circ$ , the position angle of this plane is within  $\sim 15^\circ$  of the position angles of the optical polarizations that form the ecliptic-plane-polarization-maximum.
- Wolleben (2007) has modeled the Loop I magnetic field in terms of two bubbles, one of which (S1) has expanded to the solar location. The distribution of interstellar  $\text{H}^\circ$  within 35 pc shows evidence of a shell morphology coinciding with the rims of S1. The eastern part of the shell, in ecliptic coordinates, is closest to the Sun. The upstream direction of the ISM flow past the Sun is towards the center of the S1 shell. The polarizations seen by Tinbergen are somewhat concentric with the curvature of the S1 shell for southern ecliptic regions.
- The hot and cold CMB Doppler dipole moment poles are both directed toward the boundaries of the S1 shell.
- These results suggest that the magnetic field associated with the S1 subshell of the Loop I supernova remnant creates the interstellar magnetic field at the heliosphere nose. The S1 shell dominates the polarization of stars close to the Sun, the distribution of ISM within 15 pc, the heliosphere configuration that yielded the 3 kHz emissions, and the hot and cold poles of the CMB Doppler dipole moments.
- The CMB foreground that mimics the spatial distribution of the 3 kHz emissions and the east-west heliosphere symmetry may arise from the heliosphere itself, or from another property that is also affected by the interstellar magnetic field in the S1 shell, such as the spectrum of synchrotron emission or dust grains trapped and heated in the shell.

- The polarization maximum in the ecliptic plane is dominated by five stars with the same polarization position angles. The polarization detections by Tinbergen (1982) for these stars are  $3\sigma - 5\sigma$ , and additional data on the polarization of nearby stars are desirable. Tinbergen’s data were collected during solar minimum in the mid-1970’s, and there may be a solar cycle dependence to the polarization strength.

This research has been supported by the NASA the grants NAG5-13107 and NNG05GD36G to the University of Chicago. I would like to thank Dragan Huterer for important comments on the CMB multipoles, Carl Heiles for helpful suggestions, and Hiranya Peiris, Cora Dvorkin, and Bruce Winstein for providing the ILC map data for Years 1-3 in ASCII form.

### A. Additional Information on the Polarization Data

The details of the statistics of the groups of stars averaged together to create Fig. 2 are as follows: *For the group of 129 stars that are within  $50^\circ$  of the ecliptic plane and 40 pc of the Sun:* A. Between 7 and 22 points contribute to the individual stepped central average ecliptic latitudes ( $\lambda_0$ ). B. For the 11 data points in the polarization maximum region in the interval  $\lambda \sim 280 - 310^\circ$ , between 11 and 15 stars contribute to the averaged polarization displayed at each stepped  $\lambda_0$  in ecliptic longitude. C. In this interval, the averaged polarizations are  $11.4 - 15.5 \times 10^{-5}$  degree of polarization. D. The rms variation of these averaged polarizations is  $\lesssim 8.4 \times 10^{-5}$  degree of polarization. *For the group of 51 stars that are within  $20^\circ$  of the ecliptic plane and 40 pc of the Sun:* A. Between 2 and 10 stars contribute to each data point, and 2–6 stars contribute to each data point in the  $\lambda \sim 280 - 310^\circ$  interval of the polarization maximum. B. In this interval, the averaged polarizations are  $13.0 - 21.5 \times 10^{-5}$  degree of polarization. D. The rms variation of these averaged polarizations is  $\lesssim 8.5 \times 10^{-5}$  degree of polarization.

Fig. 5 of Tinbergen (1982) shows the statistical significance of the individual data points contributing to this plot, displayed in galactic coordinates (with distances based on pre-Hipparcos distances).

The position angle of a vector is defined with respect to the north-south meridian passing through the position of the object, so that PA increases in the direction of increasing longitude. In this paper, position angles are calculated using the IDL routine `posang.pro`. Position angle transformation between coordinate systems were calculated using unweighted averages of U and Q, using the IDL function `atan(U,Q)`, which keeps track of the quadrant. If  $\theta_G$  (or  $\theta_E$ ) is the PA in the galactic (or ecliptic) coordinate system, and  $\ell_N$ ,  $b_N$  are the



galactic (or ecliptic) coordinates of the equatorial system north pole, then from Appenzeller (1968), e.g.,

$$\cot(\theta_C - \theta_G) = \frac{\cos(b) * \tan(b_N) - \cos(\ell - \ell_N) * \sin(b)}{\sin(\ell - \ell_N)} \quad (\text{A1})$$

The Tinbergen (1982) and Piirola (1977) results are consistent. Tinbergen (his Table 4) found that the mean differences in the Q and U values between the Tinbergen and Piirola surveys, for overlapping stars, are 0.3–0.6 and  $\sim 2.1 - 2.3$ , respectively, in units of  $P_5 = 10^{-5}$  degree of polarization, indicating the two data sets are in good agreement.

The stars dominating the polarization maximum within  $20^\circ$  of the ecliptic plane and near  $\lambda \sim 295^\circ$  figure HD 155885, HD 161892, HD 169916, HD 177716, and HD 181577 (Table 3). The high ecliptic latitude stars with strong polarizations are HD 137759, HD 142373, HD 150997, HD 153597, HD 163588, HD 170153, HD 185144, and HD 216228. The statistically insignificant polarization maximum seen near  $\lambda_0 \sim 140^\circ$  in Fig. 2 is dominated by the three high galactic latitude stars HD 90839, HD 95689, and HD 98230. The stars with  $P_5 > 3\sigma$  at low ecliptic latitudes are HD 205478, HD 196171, HD 209100, and HD 219571, where  $P_5 = P/10^{-5}$  degree of polarization.

For a larger spatial interval around the heliosphere nose, the position angles of the distant stars are found to vary systematically with *ecliptic* latitude. This variation is due to a coincidental alignment of a Loop I magnetic filament with  $\beta$ , and is a byproduct of the curvature of a Loop I magnetic filament that extends between  $\ell \sim 330^\circ$  and  $\ell \sim -345^\circ$ , at  $b \sim -12^\circ$ . The distance and ecliptic latitude dependencies of the galactic position angle  $\text{PA}_G$  are plotted for stars in the vicinity of the heliosphere nose in Fig. 8. The TPC stars are in the interval  $255^\circ < \lambda < 340^\circ$  and  $-35^\circ < \beta < 10^\circ$ , and the HPC stars are additionally restricted to the interval  $-18^\circ < b < 16^\circ$  and either  $\ell > 355^\circ$  or  $\ell < 5^\circ$ . The PA of HD 152424 is anomalous and the star is omitted from the plots. Fig. 8, top, shows that there is no evidence for a systematic distance dependence of  $\text{PA}_G$  with the distance of the star. In contrast,  $\text{PA}_G$  rotates towards the east (larger values) at lower ecliptic latitudes (bottom). This coincidental rotation of  $\text{PA}_G$  with ecliptic latitude shows the curvature of the magnetic field traced by distant stars that sample a filament of the Loop I supernova remnant. The best-fit first order polynomial,  $\text{PA}_G = a - b\beta$ , for the 26 HPC and TPC stars in this region with  $D < 400$  pc and  $\beta > -35^\circ$  yields  $a = 8.67 \pm 4.54$  and  $b = -2.19 \pm 0.24$  (blue line, Fig. 8, bottom). For stars within 200 pc,  $\text{PA}_G$  values can be fit with a polynomial with  $a = 28.57 \pm 5.35$  and  $b = -0.56 \pm 0.74$  (orange line, Fig. 8 bottom). Polarization measurements of additional nearby stars are required in the heliosphere nose direction to improve the comparisons between the position angles of near and distant stars.

## B. Voyager 3 kHz Emissions

Voyagers 1 and 2 observed the 3 kHz emissions during the years 1992–1994. The locations of the 3 kHz emissions are determined by triangulation with Voyagers 1 and 2, the lag time for the solar flare material to reach the outer heliosphere, and spacecraft pointing considerations that included forbidden regions in the upwind directions. The result is that each emission event has two possible locations. For simplicity, the location closest to the heliosphere nose was selected as the primary location by Kurth & Gurnett (2003), with the remaining solution selected as the ambiguous (or alternate) location. However, the true source locations may be the reverse of this assumption, or even a combination of the primary and alternate locations. The primary solutions yield emissions that are aligned parallel to the galactic plane in the upwind hemisphere, with an average galactic latitude of  $14.7^\circ \pm 7.3^\circ$ , compared to the latitude of the heliosphere nose of  $b=15.9^\circ$ . If the primary solutions for these events are assumed to form along a straight line in the galactic coordinate system, then the best fit to that line is  $b = 14.6 + 1.6 \times 10^{-3} * \ell$ . The set of 3 kHz emission locations that are best aligned with the  $\lambda = 181^\circ$  meridian consists of a combination of alternate and primary locations. The emission event locations depicted in Figures 3, 4, 7, and 6 consist of the alternate locations, except for the low latitude events of August 1993 at 2.95 kHz ( $6'$ ) and November 1993 at 3.2 kHz (7) for which the primary locations are used.

Most of the theoretical attention has been focused on the upwind solutions (e.g. Mitchell et al. 2004). The alternate locations form a pattern that samples a side-wind direction, with an average *ecliptic* longitude of  $\lambda=181.4 \pm 19.0$ . This sidewind direction is  $\sim 73^\circ$  away from the upstream meridian,  $\lambda=254.7^\circ$  (Fig. 6). Because of the coincidence of these sidewind solutions with the CMB quadrupole area vector directions (§4, Fig. 6), the sidewind locations now require theoretical attention.

## REFERENCES

- Baguhl, M., Gruen, E., & Landgraf, M. 1996, Space Science Reviews, 78, 165
- Bennett, C. L., Hill, R. S., Hinshaw, G., Nolte, M. R., Odegard, N., Page, L., Spergel, D. N., Weiland, J. L., Wright, E. L., Halpern, M., Jarosik, N., Kogut, A., Limon, M., Meyer, S. S., Tucker, G. S., & Wollack, E. 2003, ApJS, 148, 97
- Bochkarev, N. G. 1984, Large-scale Bubble Structure of the Interstellar Medium and Properties of the Local Spiral Arm, 305–310
- Breitschwerdt, D., Freyberg, M. J., & Egger, R. 2000, A&A, 361, 303

- Bruhweiler, F. C. 1984, Absorption line studies and the distribution of neutral gas in the local interstellar medium, Tech. rep.
- Burlaga, L. F., Ness, N. F., Acuña, M. H., Lepping, R. P., Connerney, J. E. P., Stone, E. C., & McDonald, F. B. 2005, *Science*, 309, 2027
- Collier, M. R., Moore, T. E., Simpson, D., Roberts, A., Szabo, A., Fuselier, S. A., Wurz, P., Lee, M. A., & Tsurutani, B. T. 2004, *Adv. Space Res.*, 34, 166
- Copi, C. J., Huterer, D., Schwarz, D. J., & Starkman, G. D. 2007, *Phys. Rev. D*, 75, 023507
- Crawford, I. A. 1991, *A&A*, 247, 183
- Crutcher, R. M. 1982, *ApJ*, 254, 82
- Czechowski, A. & Mann, I. 2003, *J. Geophys. Res.*, 108, 13
- de Geus, E. J. 1992, *A&A*, 262, 258
- Decker, R. B., Krimigis, S. M., Roelof, E. C., Hill, M. E., Armstrong, T. P., Gloeckler, G., Hamilton, D. C., & Lanzerotti, L. J. 2005, *Science*, 309, 2020
- Dehnen, W. & Binney, J. J. 1998, *MNRAS*, 298, 387
- Egger, R. J. & Aschenbach, B. 1995, *A&A*, 294, L25
- Eriksen, H. K., Hansen, F. K., Banday, A. J., Górski, K. M., & Lilje, P. B. 2004, *ApJ*, 605, 14
- Frick, P., Stepanov, R., Shukurov, A., & Sokoloff, D. 2001, *MNRAS*, 325, 649
- Frisch, P. C. 1981, *Nature*, 293, 377
- . 1995, *Space Sci. Rev.*, 72, 499
- . 2003, *ApJ*, 593, 868
- . 2005, *ApJ*, 632, L143
- Frisch, P. C., Dorschner, J. M., Geiss, J., Greenberg, J. M., Grün, E., Landgraf, M., Hoppe, P., Jones, A. P., Krätschmer, W., Linde, T. J., Morfill, G. E., Reach, W., Slavin, J. D., Svestka, J., Witt, A. N., & Zank, G. P. 1999, *ApJ*, 525, 492
- Frisch, P. C., Grodnicki, L., & Welty, D. E. 2002, *ApJ*, 574, 834

- Frisch, P. C. & York, D. G. 1983, *ApJ*, 271, L59
- Grün, E., Srama, R., Krüger, H., Kempf, S., Dikarev, V., Helfert, S., & Moragas-Klostermeyer, G. 2005, *Icarus*, 174, 1
- Grün, E., Zook, H. A., Baguhl, M., Balogh, A., Bame, S. J., Fechtig, H., Forsyth, R., Hanner, M. S., Horanyi, M., Kissel, J., Lindblad, B.-A., Linkert, D., Linkert, G., Mann, I., McDonnell, J. A. M., Morfill, G. E., Phillips, J. L., Polanskey, C., Schwehm, G., Siddique, N., Staubach, P., Svestka, J., & Taylor, A. 1993, *Nature*, 362, 428
- Gurnett, D. A., Kurth, W. S., Cairns, I. H., & Mitchell, J. 2006, in *American Institute of Physics Conference Series*, Vol. 858, *Physics of the Inner Heliosheath*, ed. J. Heerikhuisen, V. Florinski, G. P. Zank, & N. V. Pogorelov, 129–134
- Han, J. L. 2006, *Chinese Journal of Astronomy and Astrophysics Supplement*, 6, 211
- Heerikhuisen, J., Pogorelov, N. V., Zank, G. P., & Florinski, V. 2007, *ApJ*, 655, L53
- Heiles, C. 1976, *ARA&A*, 14, 1
- . 2000, *AJ*, 119, 923
- Heiles, C., Chu, Y. ., Troland, T. H., Reynolds, R. J., & Yegingil, I. 1980, *ApJ*, 242, 533
- Hinshaw, G., Nolta, M. R., Bennett, C. L., Bean, R., Doré, O., Greason, M. R., Halpern, M., Hill, R. S., Jarosik, N., Kogut, A., Komatsu, E., Limon, M., Odegard, N., Meyer, S. S., Page, L., Peiris, H. V., Spergel, D. N., Tucker, G. S., Verde, L., Weiland, J. L., Wollack, E., & Wright, E. L. 2007a, *ApJS*, 170, 288
- . 2007b, *ApJS*, 170, 288
- Holzer, T. E. 1989, *ARA&A*, 27, 199
- Kogut, A., Lineweaver, C., Smoot, G. F., Bennett, C. L., Banday, A., Boggess, N. W., Cheng, E. S., de Amici, G., Fixsen, D. J., Hinshaw, G., Jackson, P. D., Janssen, M., Keegstra, P., Loewenstein, K., Lubin, P., Mather, J. C., Tenorio, L., Weiss, R., Wilkinson, D. T., & Wright, E. L. 1993, *ApJ*, 419, 1
- Kogut, A., Smoot, G. F., Bennett, C. L., Wright, E. L., Aymon, J., de Amici, G., Hinshaw, G., Jackson, P. D., Kaita, E., Keegstra, P., Lineweaver, C., Loewenstein, K., Rokke, L., Tenorio, L., Boggess, N. W., Cheng, E. S., Gulkis, S., Hauser, M. G., Janssen, M. A., Kelsall, T., Mather, J. C., Meyer, S., Moseley, S. H., Murdock, T. L., Shafer, R. A., Silverberg, R. F., Weiss, R., & Wilkinson, D. T. 1992, *ApJ*, 401, 1

- Kurth, W. S. & Gurnett, D. A. 2003, *J. Geophys. Res.*, 108, 2
- Lallement, R., Quémerais, E., Bertaux, J. L., Ferron, S., Koutroumpa, D., & Pellinen, R. 2005, *Science*, 307, 1447
- Landsman, W. B., Henry, R. C., Moos, H. W., & Linsky, J. L. 1984, *ApJ*, 285, 801
- Linde, T. J. & Gombosi, T. I. 2000, *J. Geophys. Res.*, 105, 10411
- Linsky, J. L. & Wood, B. E. 1996, *ApJ*, 463, 254
- Möbius, E., Bzowski, M., Chalov, S., Fahr, H.-J., Gloeckler, G., Izmodenov, V., Kallenbach, R., Lallement, R., McMullin, D., Noda, H., Oka, M., Pauluhn, A., Raymond, J., Ruciński, D., Skoug, R., Terasawa, T., Thompson, W., Vallenga, J., von Steiger, R., & Witte, M. 2004, *A&A*, 426, 897
- Macek, W. M. 1990, in *Physics of the Outer Heliosphere*, ed. S. Grzedzielski & D. E. Page, 399–402
- Maíz-Apellániz, J. 2001, *ApJ*, 560, L83
- Mather, J. C., Cheng, E. S., Cottingham, D. A., Eplee, Jr., R. E., Fixsen, D. J., Hewagama, T., Isaacman, R. B., Jensen, K. A., Meyer, S. S., Noerdlinger, P. D., Read, S. M., Rosen, L. P., Shafer, R. A., Wright, E. L., Bennett, C. L., Boggess, N. W., Hauser, M. G., Kelsall, T., Moseley, Jr., S. H., Silverberg, R. F., Smoot, G. F., Weiss, R., & Wilkinson, D. T. 1994, *ApJ*, 420, 439
- Mathis, J. S. 1986, *ApJ*, 308, 281
- McClure-Griffiths, N. M., Dickey, J. M., Gaensler, B. M., Green, A. J., & Haverkorn, M. 2006, *ApJ*, 652, 1339
- McComas, D., Allegrini, F., Bartolone, L., & Frisch, P. C., e. a. 2005, *Proceedings of Solar Wind 11/SOHO 16 Conference ‘Connecting Sun and Heliosphere’*, 12-17 June 2005, Whistler, Canada ESA SP-592
- Mitchell, J. J., Cairns, I. H., & Robinson, P. A. 2004, *Journal of Geophysical Research (Space Physics)*, 109, 6108
- Nerney, S., Suess, S. T., & Schmahl, E. J. 1995, *J. Geophys. Res.*, 100, 3463
- Opher, M., Stone, E. C., & Gombosi, T. I. 2007, *Science*, 316, 875
- Perryman, M. A. C. 1997, *A&A*, 323, L49

- Pirola, V. 1977, A&AS, 30, 213
- Pogorelov, N. V., Zank, G. P., & Ogino, T. 2004, ApJ, 614, 1007
- Quémerais, E., Bertaux, J.-L., Lallement, R., Berthé, M., Kyrölä, E., & Schmidt, W. 2000, Advances in Space Research, 26, 815
- Redfield, S. & Linsky, J. L. 2004, ApJ, 602, 776
- Riegel, K. W. & Crutcher, R. M. 1972, A&A, 18, 55
- Schwarz, D. J., Starkman, G. D., Huterer, D., & Copi, C. J. 2004, Physical Review Letters, 93, 221301
- Slavin, J. D. & Frisch, P. C. 2007, A&A, submitted, 000, 0000
- Smoot, G. F., Bennett, C. L., Kogut, A., Wright, E. L., Aymon, J., Bogges, N. W., Cheng, E. S., de Amici, G., Gulkis, S., Hauser, M. G., Hinshaw, G., Jackson, P. D., Janssen, M., Kaita, E., Kelsall, T., Keegstra, P., Lineweaver, C., Loewenstein, K., Lubin, P., Mather, J., Meyer, S. S., Moseley, S. H., Murdock, T., Rokke, L., Silverberg, R. F., Tenorio, L., Weiss, R., & Wilkinson, D. T. 1992, ApJ, 396, L1
- Smoot, G. F., Gorenstein, M. V., & Muller, R. A. 1977, Physical Review Letters, 39, 898
- Spitzer, L. 1978, Physical Processes in the Interstellar Medium (New York: John Wiley & Sons, Inc.)
- Stone, E. C. 2007, AGU Fall Meeting Abstracts, A1+
- Stone, E. C., Cummings, A. C., McDonald, F. B., Heikkilä, B. C., Lal, N., & Webber, W. R. 2005, Science, 309, 2017
- Tinbergen, J. 1982, A&A, 105, 53
- Washimi, H. & Tanaka, T. 1996, Space Sci. Rev., 78, 85
- Weingartner, J. C. 2004, in Astronomical Society of the Pacific Conference Series, Vol. 309, Astrophysics of Dust, ed. A. N. Witt, G. C. Clayton, & B. T. Draine, 453–+
- Weller, C. S. & Meier, R. R. 1974, ApJ, 193, 471
- Witte, M. 2004, A&A, 426, 835
- Wolleben, M. 2007, ApJ, 664, 349

- Wood, B., Müller, H., Zank, G., & Linsky, J. 2002, ApJ, 574, 412
- Wood, B. E., Redfield, S., Linsky, J. L., Müller, H.-R., & Zank, G. P. 2005, ApJS, 159, 118
- Wurz, P., Collier, M. R., Moore, T. E., Simpson, D., Fuselier, S., & Lennartson, W. 2004, in American Institute of Physics Conference Series, Vol. 719, Physics of the Outer Heliosphere, ed. V. Florinski, N. V. Pogorelov, & G. P. Zank, 195–200
- Zurbuchen, T. H. 2007, ARA&A, 45, 297

Table 1. Position Angles

Item	PA <sub>G</sub>	PA <sub>E</sub>	Notes
Tinbergen (1982) <sup>A</sup>	$35 \pm 4$	$-25 \pm 4$	Five upwind stars within 40 pc and $P_5 \geq 17.5$
Heiles (2000) <sup>B</sup>	$41 \pm 20$	$-20 \pm 20$	Stars near polarization maximum and at 140–240 pc
CMB dipole moment <sup>C,D</sup>	$50^\circ \pm 1^\circ$	$-11^\circ \pm 1^\circ$	5.0° from He° upwind
H°- He° offset <sup>D</sup>	$27^\circ \pm 14^\circ$	$-33^\circ \pm 14^\circ$	

<sup>A</sup>Position angle averages are calculated for stars in the interval  $260^\circ < \lambda < 305^\circ$ ,  $-25^\circ < \beta < 10^\circ$

<sup>B</sup>Position angle averages are calculated for stars in the interval  $260^\circ < \lambda < 305^\circ$ ,  $-25^\circ < \beta < 10^\circ$  and  $335 < \ell < 360^\circ$ ,  $-18^\circ < b < 10^\circ$ .

<sup>C</sup>Position angles represent the position angle of the plane that is equidistant between the two poles of the CMB dipole moment, for the location  $\lambda \sim 260.3^\circ$ ,  $\beta \sim +6.6^\circ$ , which is the closest point of the this plane to the He° upstream direction. Th is plane separates the hot and cold hemispheres of the CMB Doppler dipole moment.

<sup>D</sup>Position angles are calculated using the IDL routine posang.pro, which gives the position angle of point 2 with respect to a great circle meridian passing through point 1.



Table 2. Summary of Directions

Direction	$\ell, b$	$\lambda, \beta$	Ref.
Tinbergen Polarization Max.	$\sim 19.2^\circ, \sim -21.2^\circ$	$294^\circ \pm 10^\circ, 0^\circ \pm 20^\circ$	§2.1
He <sup>o</sup> upwind (LIC)	$3.5^\circ + 15.2^\circ$	$255.4^\circ \pm 0.5^\circ, 5.1^\circ \pm 0.5^\circ$	1
H <sup>o</sup> upwind	$5.8^\circ, +19.3^\circ$	$252.9^\circ \pm 0.5^\circ, 9.0^\circ \pm 0.5^\circ$	2
CMB dipole hot pole	$263.9^\circ, 48.3^\circ$	$171.6, -11.1$	3
CMB dipole plane to upstream <sup>A</sup>	$6.9^\circ \pm 0.5^\circ, 11.4^\circ \pm 0.1^\circ$	$260.4^\circ \pm 0.5^\circ, 6.1^\circ \pm 0.5^\circ$	3
ISM Dust upwind	$263.9^\circ, 48.3^\circ$	$259^\circ \pm 10^\circ, 8^\circ \pm 5^\circ$	4
LIC LSR upstream	$346^\circ, -1^\circ$	$260^\circ, -18^\circ$	5
CLIC LSR upstream	$0^\circ, -5^\circ$	$271^\circ, -8^\circ$	5

References. — 1. Witte (2004, and private communication). 2. Lallement et al. (2005). 3. This paper and Hinshaw et al. (2007b)[Hinshaw 2007 reference] 4. Frisch et al. (1999). 5. Frisch et al. (2002), for solar apex motion from Dehnen & Binney (1998).

<sup>A</sup>This plane is equidistant between the hot and cold poles of the CMB dipole moment.

Table 3. Stars Dominating Ecliptic Polarization

HD	Dist.	$P_5$	$PA_E$
155885 (36 Oph)	6	17.5	$-20^\circ$
161892	39	25.5	$-25^\circ$
169916 ( $\lambda$ Sgr)	24	17.5	$-27^\circ$
177716 ( $\tau$ Sgr)	37	21.2	$-29^\circ$
181577 ( $\rho^1$ Sgr)	37	21.9	$-25^\circ$

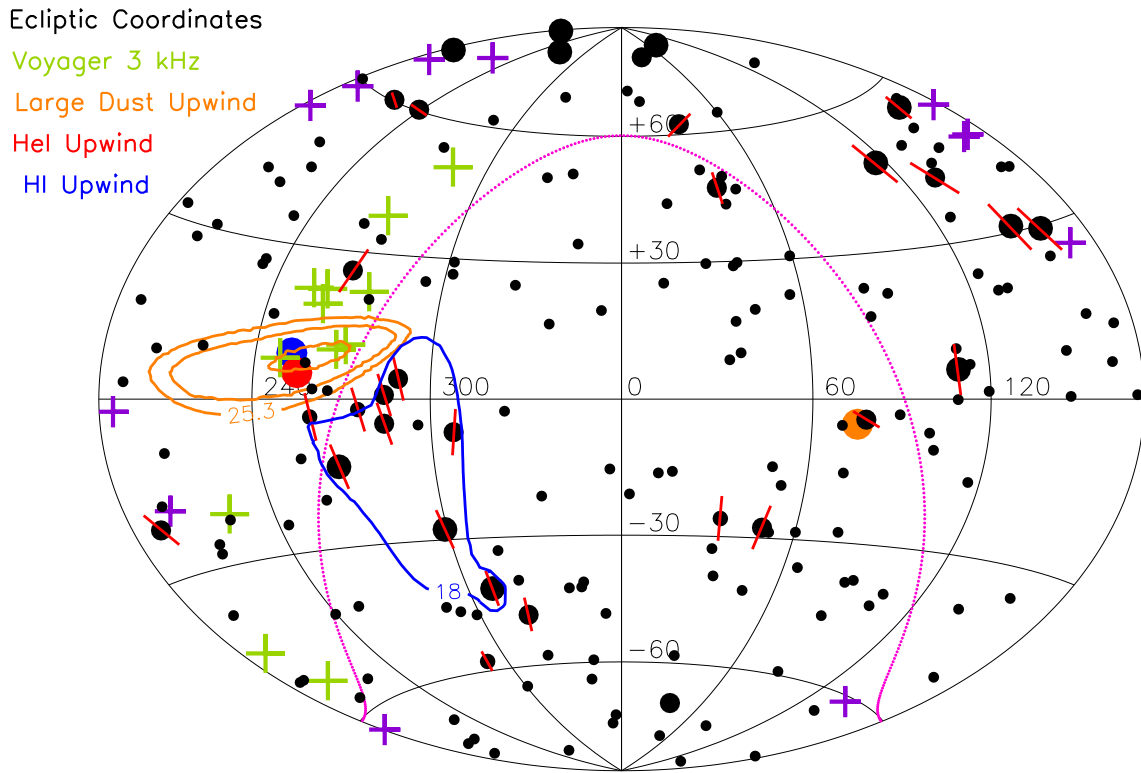


Fig. 1.— The polarizations of the TPC stars within 45 pc are plotted in ecliptic coordinates using an Aitoff projection. The blue contour outlines the locations of stars near  $\lambda \sim 280^\circ$  with polarization  $> 0.018\%$ , and the red lines show the direction of the polarization plane of vibration. The heliosphere nose direction is defined by the upwind directions of interstellar  $\text{He}^0$  (red dot), and the  $\text{H}^0$  and downwind  $\text{He}^0$  directions are also shown (blue, and orange dots). Orange contours show the 1- $\sigma$ , 2- $\sigma$ , and 3- $\sigma$  uncertainties on the upwind direction of large interstellar dust grains (typically radii  $\gtrsim 0.2 \mu\text{m}$ ) flowing into the heliosphere (Frisch et al. 1999). The primary locations of the 3 kHz emission events detected by the Voyager satellites are plotted as light green crosses, and the purple crosses show the ambiguous alternate locations (Appendix B). The pink dotted line shows the galactic plane. The region of enhanced polarization extends to negative ecliptic latitudes. Small, medium and large dots indicate stars with polarizations of 15–19, 19–23, and over  $23 \times 10^{-5}$  degree of polarization, respectively.

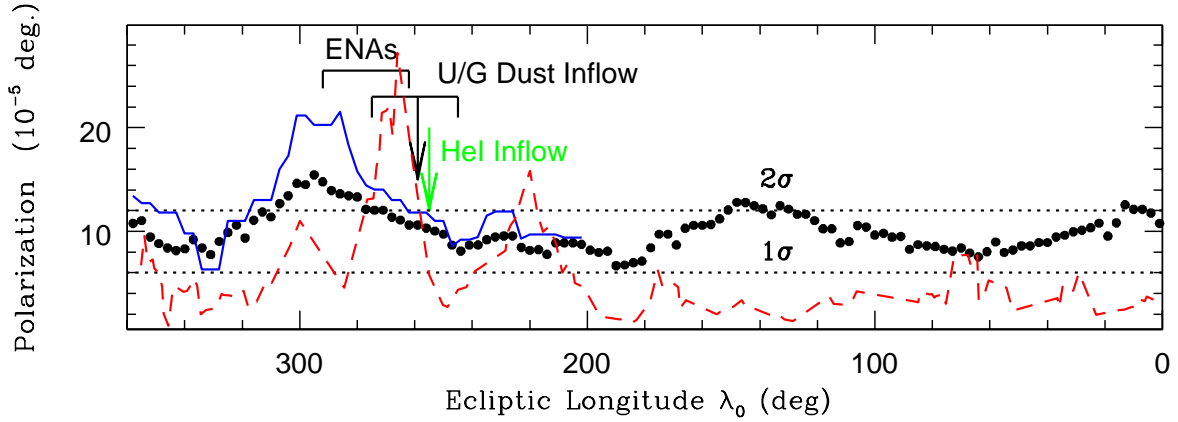


Fig. 2.— Polarization properties as a function of ecliptic longitude: The blue line shows the averaged polarizations  $P$  for stars with  $|\beta| < 20^\circ$ , and the dots indicate averaged values for stars with  $|\beta| < 50^\circ$  in the TPC. The  $1\sigma$  and  $2\sigma$  polarization uncertainties are shown (from Tinbergen 1982). The polarization data for nearby stars in the TPC are averaged over  $\pm 20^\circ$  in ecliptic longitude,  $\lambda$ . The direction of maximum  $P$  is shifted by  $\sim 30^\circ$  from the upwind direction of interstellar dust grains flowing through the heliosphere, and by  $\sim 40^\circ$  from the  $\text{He}^\circ$  upwind direction. The black arrow shows the upstream direction, and  $1\sigma$  uncertainties, for interstellar dust flowing through the heliosphere based on Ulysses and Galileo data (F99). The green arrow shows the upstream direction from observations of interstellar  $\text{He}^\circ$  in the inner heliosphere (from Witte 2004). The upwind direction of the ENA flux originating in the outer heliosphere is indicated (from Collier et al. 2004; Wurz et al. 2004). The red dashed line shows the relative polarizations of 184 stars in the HPC (Heiles 2000), with  $|\beta| < 20^\circ$  and 40–100 pc from the Sun. The polarization strengths of the HPC data are reduced by a factor of 20 for comparison with the TPC data, and are averaged over an interval of  $\pm 5^\circ$  around the central ecliptic longitude. The two strongest maximum in the HPC data are where the sightline crosses the North Polar Spur (strongest peak,  $\ell, b \sim 4^\circ, 4^\circ$ ) and towards an  $\text{H}^\circ$ -21 cm filament that is part of the Egger interaction ring ( $\ell, b \sim 336^\circ, 42^\circ$ , Egger & Aschenbach 1995).

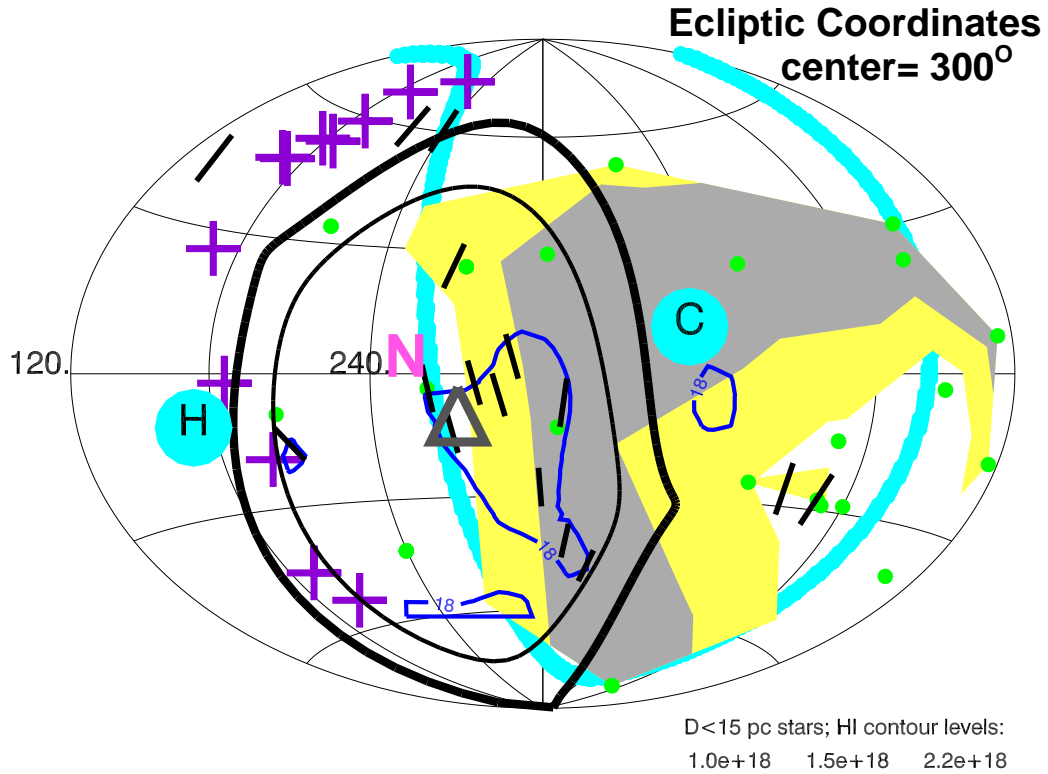


Fig. 3.— The distribution of interstellar  $\text{H}^{\circ}$  within 15 pc is plotted in the ecliptic coordinate system. The plot is centered at  $\lambda = 300^{\circ}$ . Stars within 15 pc are used to define the distribution of local ISM with  $N(\text{H}^{\circ}) > 1 \times 10^{18} \text{ cm}^{-2}$ . The polarizations of stars in the TPC with  $P_5 > 18$  are plotted as black bars, and the dark blue contour line shows the contour around these values. The levels of the filled yellow and gray  $N(\text{H}^{\circ})$  contours are listed in the plot, and green dots show the positions of the stars used to define the contours. The data are from Wood et al. (2005) and Redfield & Linsky (2004), with  $\text{D}/\text{H} = 1.5 \times 10^{-5}$  in some cases. Large cyan-colored dots with “H” and “C” over-plotted show, respectively, the hot and cold poles of the CMB Doppler dipole moment. The cyan-colored line divides the hot and cold hemispheres of the CMB Doppler dipole moment. The purple crosses show the locations of the 3 kHz emissions seen by the Voyager satellites (see text and Appendix B). The large concentric “circles” show the inner and outer boundaries of the “S1” magnetic loop, which is part of the Loop I magnetic bubble that has expanded to the solar location (Wolleben 2007; Frisch 1981). The gray triangle shows the upwind direction of the CLIC in the LSR for an assumed solar apex motion corresponding to the Hipparcos-based value (Frisch et al. 2002). The heliosphere nose direction, according to interstellar  $\text{He}^{\circ}$  flowing into the heliosphere, is marked by the large pink “N”.

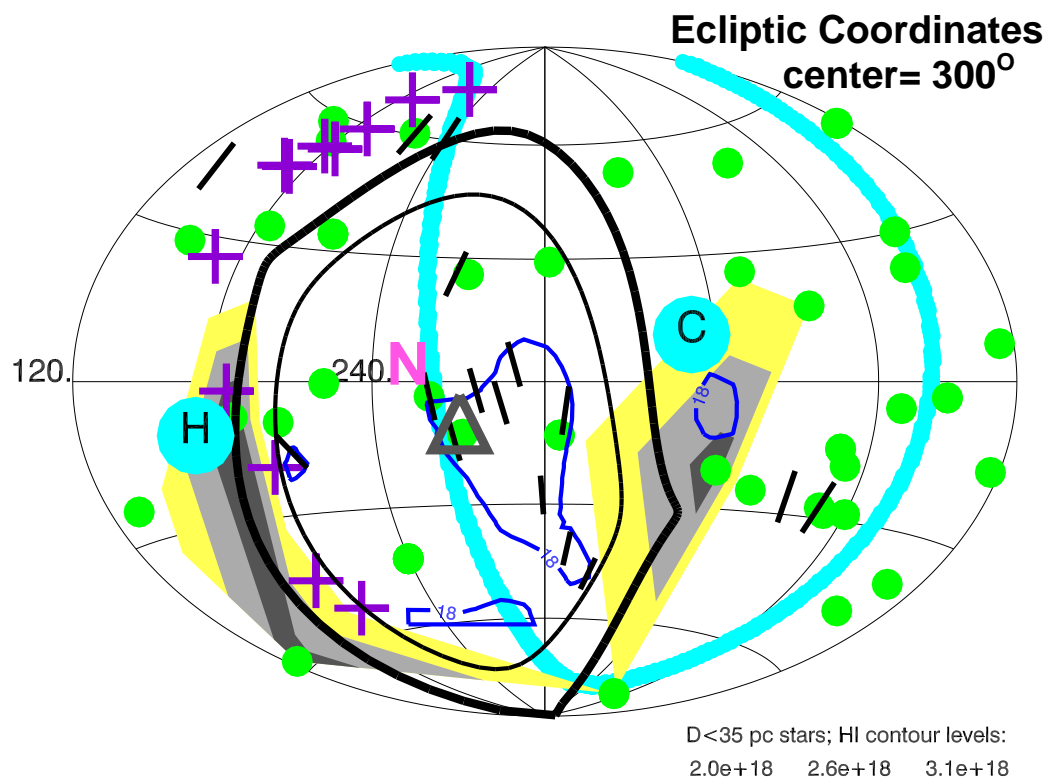


Fig. 4.— Same as Fig. 3, but for stars within 35 pc.

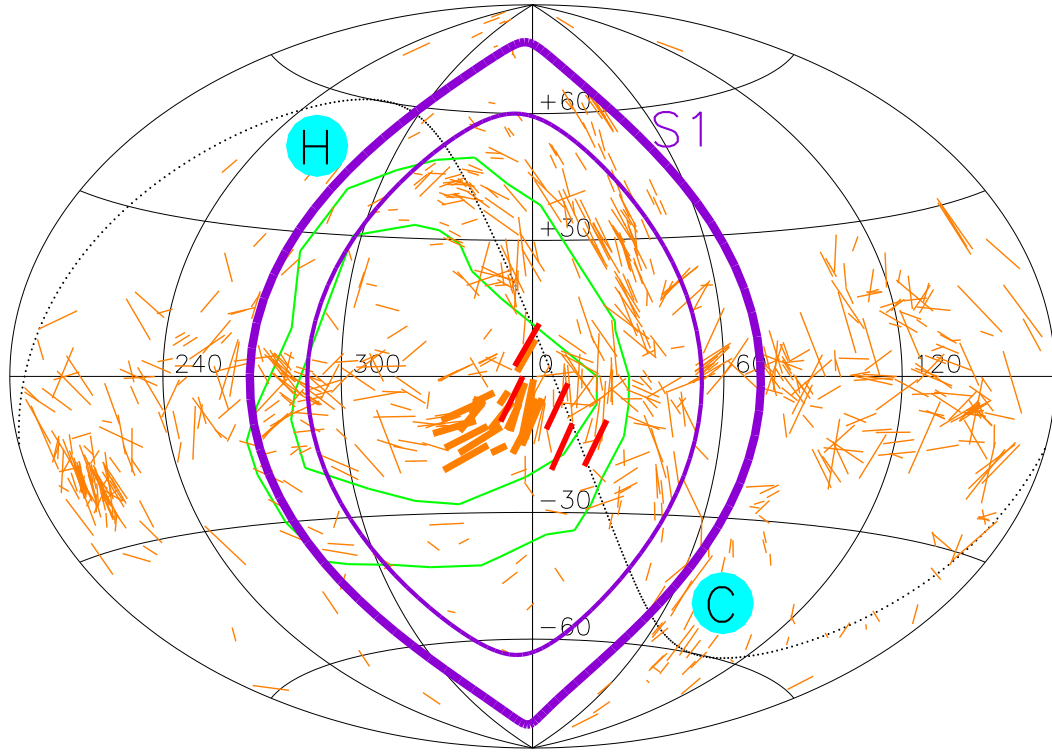


Fig. 5.— Polarization data for stars within 250 pc from Heiles (2000, orange bars), and polarizations of nearby stars in the TPC that form the polarization maximum in the ecliptic plane (red bars, §2.1). The figure is an Aitoff projection with galactic coordinates. The S1 subshell of the Loop I magnetic bubble is indicated (purple lines, Wolleben 2007), as is the ring attributed to the interaction of the Loop I and Local Bubble (green circles, Egger & Aschenbach 1995). The H and C symbols and cyan-colored dots indicate the hot and cold poles of the CMB dipole moment. The near and far ISM yield the same position angles, to within uncertainties, indicating that Loop I dominates the large-scale magnetic field structure in the upwind direction.

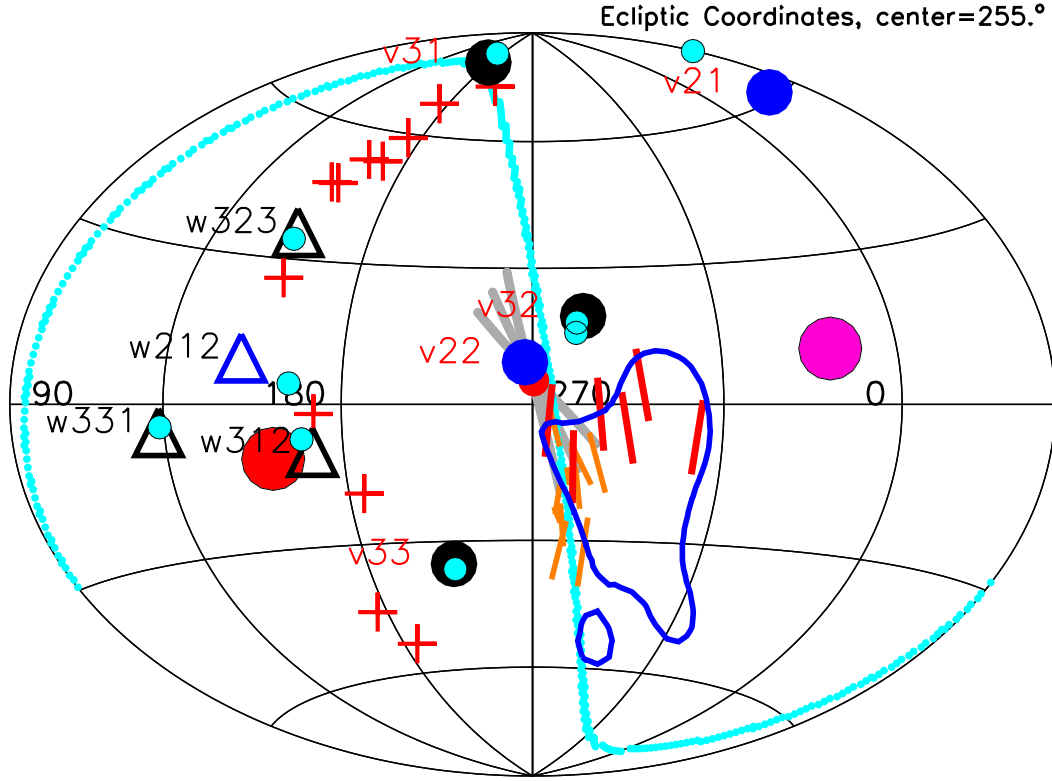


Fig. 6.— The positions of ILC123 multipole vectors  $\hat{v}$  and area vectors  $\vec{w}$ , that carry the phase information about the CMB power for  $\ell = 2$  and  $\ell = 3$ , are plotted in ecliptic coordinates (from Copi et al. 2007, Table 1, ILC123 data). The quadrupole multipole vectors  $v^{21}$  and  $v^{22}$  (filled blue dots), and area vector  $w^{212}$  are the blue dots and triangle. The octopole multipole vectors  $v^{31}$ ,  $v^{32}$ , and  $v^{33}$  and area vectors,  $w^{312}$ ,  $w^{323}$ ,  $w^{331}$ , are plotted as black dots and triangles, respectively. The other symbols are the same as in Fig. 7. The  $v^{22}$  multipole vector coincides with the heliosphere nose direction. The multipoles for the ILC1 map (from Table 1, Copi et al., 2007) are plotted as small cyan dots. The four area vectors (normals to planes formed by multipole pairs) and the hot pole of the CMB dipole are all located towards the sidewind band defined by the 3 kHz emissions. The 3 kHz emissions are formed where outward propagating global merged interaction regions interact with the magnetically-shaped heliopause (Mitchell et al. 2004). The coincidence of the area vectors with the 3 kHz emission band suggests that the ecliptic coordinate system is felt by the low- $\ell$  moments of the CMB because of the shaping of the heliosphere by the interstellar magnetic field. The plot is in ecliptic coordinates and is centered on the heliosphere nose at  $\lambda \sim 255^\circ$ .



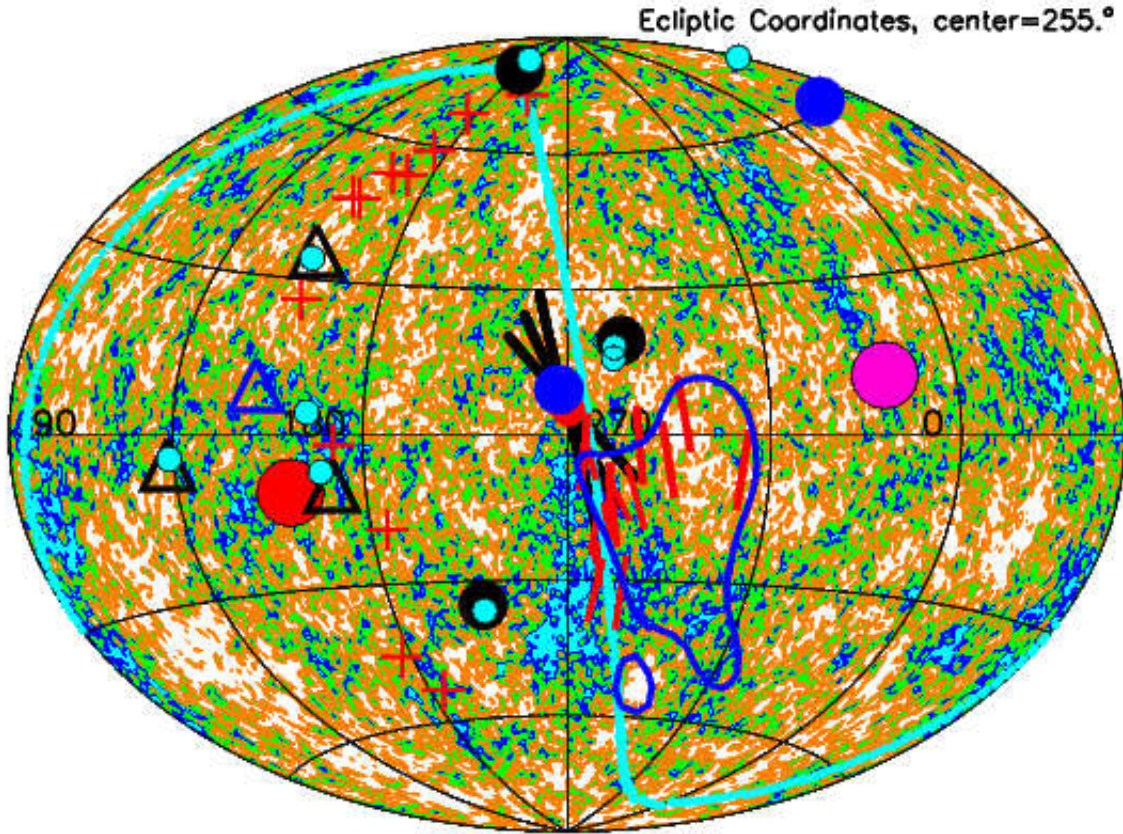


Fig. 7.— The WMAP Internal Linear Combination for Years 1-3 is displayed in the ecliptic coordinate system, and shifted by  $105^\circ$  so that the LIC upwind direction is at the plot center. Ecliptic longitude is labeled, and increases to the right. The large red (pink) dot shows the maximum (minimum) temperature of the CMB dipole moment (Table 2). The thick cyan line shows the plane that is equidistant between the CMB dipole temperature maximum and minimum. The small partially hidden red dot shows the observed upwind direction of interstellar gas and large dust grains flowing into the heliosphere. The three thick black lines show the offset angle, and uncertainties on that angle, between the inflow directions of interstellar  $\text{He}^{\text{I}}$  and  $\text{H}^{\text{I}}$ . The red bars show the stellar polarizations from Fig. 6. The red crosses show the positions of the 3 kHz emission events (Appendix B). The CMB data temperature scale is:  $dT$ :  $< -0.119$  (cyan),  $-0.082$  to  $-0.055$  (blue),  $-0.055$  to  $0.0$  (green),  $0$  to  $0.055$  (orange),  $> 0.055$  (white), where the temperature  $dT$  is in mK.



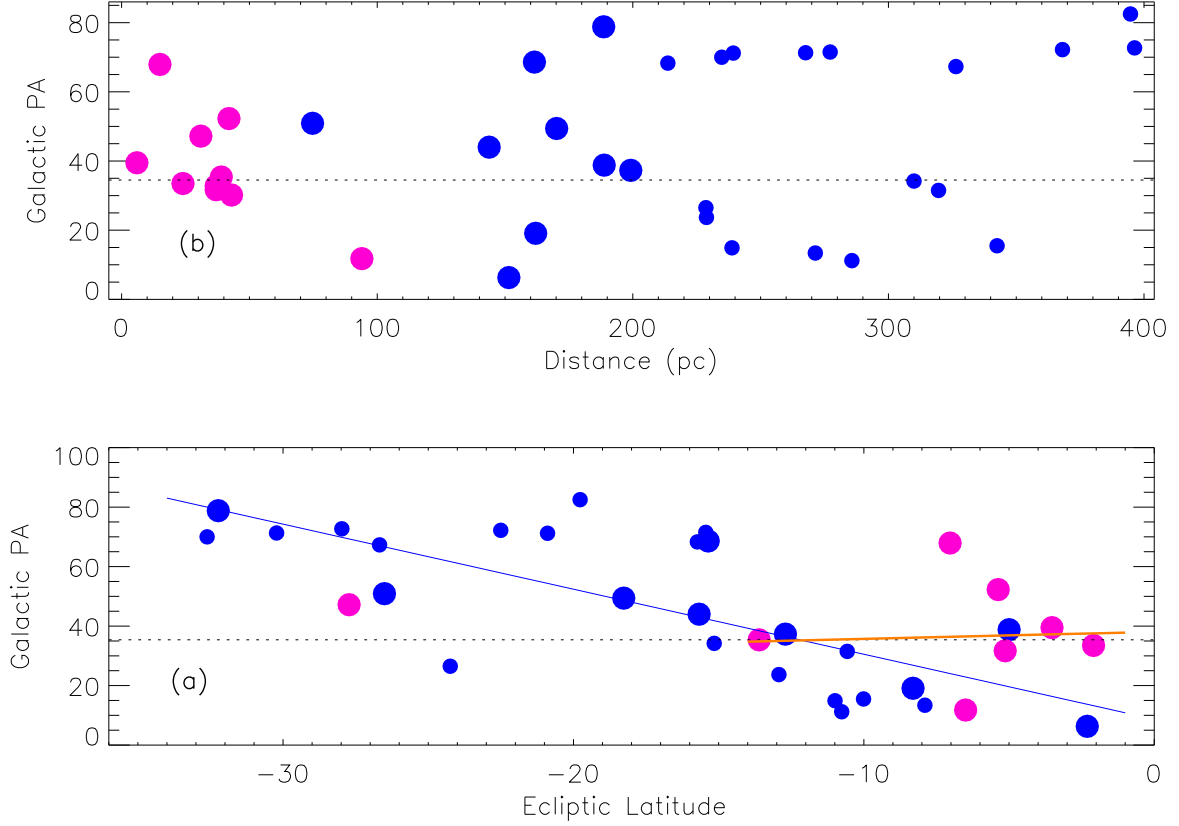


Fig. 8.— Position angles in galactic coordinates ( $PA_G$ ) are plotted against the ecliptic latitude (a) and star distance (b) for stars at negative ecliptic latitudes in the heliosphere nose region (Appendix A). Large (small) symbols indicate stars with distances  $D < 200$  pc ( $D = 200 - 400$  pc). Blue (pink) symbols indicate stars from the HPC (TPC). The  $PA_G$  values for nearby stars,  $D < 200$  pc, is relatively constant close to the ecliptic plane,  $-15^\circ < \beta < 0^\circ$ , with a value close to the  $PA_G$  of the  $H^0$ - $He^0$  offset angle (dotted lines). The  $PA_G$  values of distant stars show no dependence on distance, but a strong dependence on ecliptic latitude that traces the curvature of the magnetic field in the Loop I superbubble in this region. The blue line in (a) shows a first order polynomial fit to the latitude dependence of  $PA_G$  for HPC stars in this region,  $D < 400$  pc and  $-35 < \beta < 0^\circ$ . The orange line indicates a first order polynomial fit to the latitude dependence of  $PA_G$  for nearby TPC and HPC stars,  $D < 200$  pc and  $-15 < \beta < 0^\circ$ . The dotted lines give the galactic position angle of the  $H^0$ - $He^0$  offset angle. Region selection boundaries and the polynomial coefficients are given in Appendix A.